t

Spark plasma sintering as a reactive sintering tool for the preparation of surface-tailored Fe–$FeAl_2O_4$–Al_2O_3 nanocomposites

J. Gurt Santanach, C. Estournès, A. Weibel, A. Peigney, G. Chevallier and Ch. Laurent*

Université Paul-Sabatier, UMR CNRS-UPS-INP 5085, CIRIMAT, Bât. 2R1, 118 route de Narbonne, 31062 Toulouse cedex 9, France

$Al_{1.86}Fe_{0.14}O_3$ powders were partially or totally reduced in H_2. The fully reduced Fe–Al_2O_3 nanocomposite powder was sintered by spark plasma sintering (SPS) without any reaction taking place. For the other powders, the SPS induced the formation of $FeAl_2O_4$ and sometimes Fe. The most severe reducing conditions were found at the surface of the materials, producing nanocomposites with a surface layer composition and microstructure different to those of the core. This in situ formed composite layer confers a higher hardness and fracture strength.

Keywords: Spark Plasma Sintering; Scanning Electron Microscopy (SEM); Alumina; Nanocomposite

Spark plasma sintering (SPS) [1] is a rapidly developing technique. It has several advantages over pressureless sintering and hot-pressing, including lower sintering temperatures and shorter holding times. SPS typically differs from hot-pressing by a higher heating rate and the application of a current to the pressing die and sample. The temperature and current are not independent parameters and it may be difficult to separate the intrinsic role of the current from its thermal effect, i.e., Joule heating. Most previous papers [2–9] have reported results on the densification of nanomaterials with little grain growth and on materials bonding, with or without a reaction at the interface. In this paper, we study for the first time the SPS behavior of nanocomposite powders where Fe nanoparticles are dispersed in Al_2O_3 grains [10,11]. Such materials sintered by hot-pressing show a markedly higher strength and toughness than Al_2O_3 [12,13]. Moreover, as SPS is a reducing process [14], the potential for reactive sintering is investigated, with the aim of tailoring the surface composition of the material.

A powder of α-$Al_{1.86}Fe_{0.14}O_3$ solid solution (corundum-type structure) was prepared by the mixed-oxalate precipitation/calcination route [10]. The calcination (air, 1200 °C, 2 h) produced a powder in which micrometric grains presenting a vermicular microstructure form agglomerates 15–20 μm in size. The Brunauer–Emmett–Teller (BET) specific surface area is equal to 2.3 $m^2\ g^{-1}$. The powder was divided into four batches, three of which were reduced in pure H_2 in order to produce Fe–Al_2O_3 nanocomposite powders, in which nanometric Fe particles are dispersed in the oxide matrix [10,11]. Different experimental conditions (maximum temperature/dwell time = 1050 °C/5 h, 1200 °C/0.5 h and 1300 °C/1 h) were used in order to obtain different reduction yields of the Fe^{3+} ions of the starting solid solutions and therefore different metallic Fe proportions in the nanocomposite powders. The powders thus obtained were studied by thermogravimetric analysis (TGA, Setaram TAG 24) in flowing air up to 1400 °C (heating rate 3 °C min^{-1}) in order to oxidize the Fe nanoparticles and therefore determine the proportion of Fe and the reduction yield of the solid solution. The thermograms (not show) show that oxidation occurs in several steps at about 400, 850 and 1200 °C. It has been shown previously [15] that the first step corresponds to the oxidation into Fe_2O_3 of the Fe nanoparticles located on the surface of the oxide grains, whereas the latter two steps correspond to the oxidation into Fe_2O_3 of the Fe nanoparticles located within the oxide matrix grains. A fully reduced powder would consist of 7 wt.% Fe–Al_2O_3 and the total oxidation of iron would yield a weight gain equal to 2.68 wt.%. A comparison of the experimental weight gains with this figure gives reduction yields of 22, 72 and 100% for the powders reduced at 1050, 1200 and 1300 °C, respectively. These powders will hereafter be called R22, R72 and R100, respectively; accordingly,

* Corresponding author. E-mail: laurent@chimie.ups-tlse.fr

doi:10.1016/j.scriptamat.2008.09.034

the unreduced powder is R0. A summary of these results and the composition of the oxide matrix derived therefrom is given in Table 1.

X-ray diffraction (XRD) patterns (Cu K_α radiation, Bruker D4 Endeavor, not shown) reveal only peaks typical of the corundum-type oxide for all powders and also the main diffraction peak of α-Fe for R22, R72 and R100, with increasing proportions. Note that it has been shown previously [16] that the reduction of Fe^{3+} into metallic Fe occurs in one step if the reduction temperature is equal to or higher than 1000 °C, as for the present powders, whereas a $FeAl_2O_4$ spinel is formed at the interface between the intragranular Fe particles and the matrix for reduction temperatures lower than 1000 °C. Therefore, there is no $FeAl_2O_4$ in the present powders. The powders were observed by field-emission-gun scanning electron microscopy (FEG-SEM, JEOL JSM 6700 F) and transmission electron microscopy (TEM, JEOL JEM 1011). A typical FEG-SEM image (Fig. 1a) reveals the oxide matrix grains with some surface Fe nanoparticules 50–90 nm in diameter (arrowed on Fig. 1a). Typical TEM images reveal Fe nanoparticules about 20 nm in diameter (arrowed on Fig. 1b) located in the pores of the matrix and still smaller (<5 nm) nanoparticules (Fig. 1b and c), which are extremely numerous. Although such images do not allow one to determine if the latter nanoparticles are at the surface or within the oxide grains, an earlier electron microdiffraction study [16] revealed that virtually all are within, i.e., in an intragranular position.

The four powders were consolidated by SPS (Dr Sinter 2080, SPS Syntex Inc., Japan). They were loaded into an 8 mm inner diameter graphite die. A sheet of graphitic paper was placed between the punch and the powder as well as between the die and the powder for easy removal. This ensemble is known as the stack. The powders were sintered in vacuum (residual cell pressure <5 Pa). A pulse configuration of 12 pulses (each pulse was 3.3 ms in duration) followed by two periods (6.6 ms) of zero current was used. Heating rates of 150 and 100 °C min^{-1} were used from room temperature to 600 °C and from 600 to 1350 °C, respectively. An optical pyrometer, focused on a little hole at the surface of the die, was used to measure the temperature. A uniaxial pressure of 100 MPa was applied during the 600–1350 °C ramp where a dwell time of 3 min was applied. The cooling rate was 100 °C min^{-1}. The uniaxial pressure was gradually released during cooling. The sintered specimens, designated R0 S, R22 S, R72 S and R100 S in the following, were in the form of pellets 8 mm in diameter and about 2 mm thick. The density was determined using Archimedes method after removal of the graphitic surface contamination layer by light polishing. The density is in the range 4.0–4.1 for all specimens, which corresponds to a densification in the range 98–100%. The materials were cut in their middle along the pressing axis using a diamond blade and were polished up to a 1 μm diamond suspension. Interestingly, the color of the outer part (gray) and the core (green) of these cross-sections are different for R0S, R22S and R72S. By contrast, R100S is uniformly gray. The outer part will be referred to as the surface in the following. The XRD pattern of the surface of R0S (Fig. 2) reveals the peaks of three species. Indeed, besides the corundum-type phase (major phase), there is a spinel-type phase ($FeAl_2O_4$) with relatively intense peaks and metallic Fe (very minor).

The specimen was ground to remove the surface layer and the corresponding XRD pattern only reveals the corundum and spinel peaks, the latter ones being much less intense than in the surface XRD pattern. The specimen was ground some more and the XRD patterns now reveal only trace amounts of spinel besides the corundum phase. These findings are in broad agreement with the visual observations, the $FeAl_2O_4$ spinel contributing to the green color and metallic Fe to the gray one. As the starting R0 powder is a corundum-type oxide (α-$Al_{1.86}Fe_{0.14}O_3$), these results clearly show that some reduction reactions did occur during the SPS process and that it

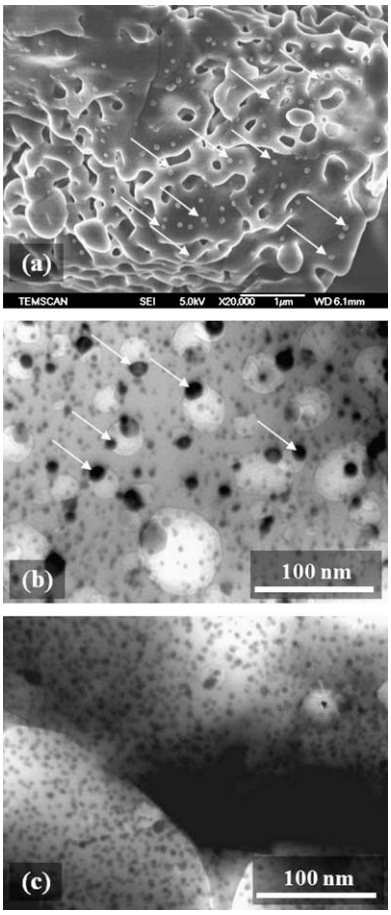

Figure 1. FEG-SEM (a) and TEM (b and c) images of a Fe–Al_2O_3 nanocomposite powder.

Table 1. Experimental conditions for the reduction in H_2: maximum temperature (T) and dwell time (t) at T; reduction rate (R) and composition of the powders as deduced from TGA.

Powder	T (°C)	t (h)	R (%)	Composition
R0	–	–	0	$Al_{1.86}Fe_{0.14}O_3$
R22	1050	5	22	1.5 wt.% Fe–$Al_{1.89}Fe_{0.11}O_3$
R72	1200	0.5	72	5 wt.% Fe–$Al_{1.96}Fe_{0.04}O_3$
R100	1300	1	100	7 wt.% Fe–Al_2O_3

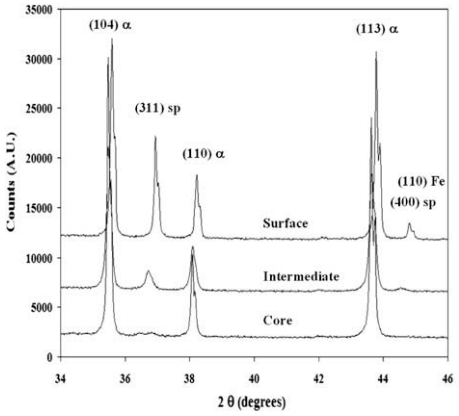

Figure 2. XRD patterns for specimen R0S at different depth (surface, intermediate and core) into the material α, corundum; sp, spinel.

was less pronounced at the core of the material. It is proposed that this is due to the insulating nature of the material, which does not allow the electron flow to pass through the core, whereas the surface is obviously closer to the conducting graphite die and punches. This is in agreement with earlier studies on the SPS of Al_2O_3 [17,18] and on the modelling of the current density along the stack [19]. Similar XRD patterns were obtained for R22S, but the Fe peak is more intense in the surface pattern than for R0S. For R72S, it is still more intense. Moreover, the Fe diffraction peak is still detected in the core XRD pattern. For R100S, all three XRD patterns show only the corundum and Fe peaks. FEG-SEM observations (Fig. 3) of a cross-section of the materials confirm that the surface and core are different, in R0S (Fig. 3a), R22S (Fig. 3b) and R72S (Fig. 3c), and reveal that the surface/core transition is fairly sharp,

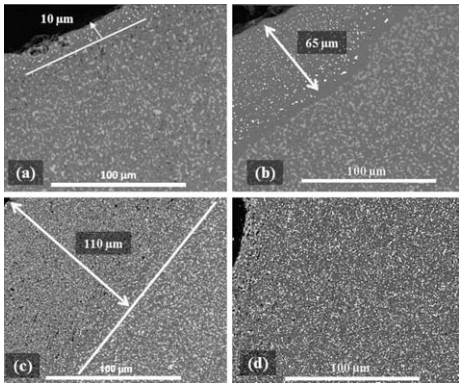

Figure 3. FEG-SEM images of a cross-section of the nanocomposites prepared by SPS: (a) R0S, (b) R22S, (c) R72S and (d) R100S.

which could be related to a limit in the distribution of the current lines in the material. In such images (backscattered electron images in chemical composition mode), the Fe particles appear as white dots and the spinel phase as light-gray particles on a dark-gray background of the corundum-phase matrix. The Fe particles are isotropic with a diameter in the range 0.5–0.8 μm. The spinel grains are elongated with a length in the range 0.6–2.5 μm. The surface layer extends to a depth of 10, 65 and 110 μm for R0S, R22S and R72S, respectively. The R100S material (Fig. 3d) homogeneously consists of the Fe–Al_2O_3 nanocomposite and indeed no further reduction could have taken place during SPS because the corresponding R100 powder was already fully reduced. The XRD and FEG-SEM results are summarized in Table 2.

From the above results, it is proposed that the phenomena described in the following take place during the SPS process (for the sake of simplicity, the non-reduced and partially reduced corundum phases are written as $Al_{2-2x}Fe_{2x}O_3$). For R0S, there was no metallic Fe in the corresponding powder. Thus, reaction (1) takes place within all the material, and either one or both reactions (2) and (3) further takes place in the surface layer.

$$Al_{2-2x}Fe_{2x}O_3 \rightarrow 2xFeAl_2O_4 + (1-3x)Al_2O_3 + x/2O_2 \quad (1)$$

$$FeAl_2O_4 \rightarrow Fe + Al_2O_3 + 1/2O_2 \quad (2)$$

$$Al_{2-2x}Fe_{2x}O_3 \rightarrow 2xFe + (1-x)Al_2O_3 + 3x/2O_2 \quad (3)$$

By contrast, metallic Fe was present in the R22 and R72 powders, in a quantity over three times higher for the latter. It is no longer detected at the core for R22S, whereas it is for R72S. It is thus proposed that, in addition to reaction (1), a reaction involving a retro-dismutation of iron, Fe(0) + Fe(III) → Fe(II), takes place at the core. For R22S, Fe is totally reacted in the core and reaction (4) could be written as:

$$Al_{2-2x}Fe_{2x}O_3 + aFe \rightarrow bFeAl_2O_4 + cAl_{2-2y}Fe_{2y}O_3 \quad (4)$$

where a, b, c are suitable coefficients and $y < x$. By contrast, for R72S, it is the source for Fe^{3+} ions ($Al_{2-2x}Fe_{2x}O_3$) that is depleted first and reaction (5) could be written as:

$$Al_{2-2x}Fe_{2x}O_3 + dFe \rightarrow eFe + fFeAl_2O_4 + gAl_2O_3 \quad (5)$$

where d, e, f, g are suitable coefficients and $e < d$.

For R100S, there were no Fe^{3+} ions in the corresponding powder and thus neither reactions (1) nor (4) can take place. There is simply no reaction during the

Table 2. Composition (w = weak) and thickness (d) of the surface layer, composition of the core, fracture strength (σ_f), toughness (K_{Ic}) and Vickers microhardness (HV) for the nanocomposite materials prepared by SPS.

	Material surface composition	d (μm)	Core composition	σ_f (MPa)	K_{Ic} (MPa m$^{1/2}$)	HV
R0S	Fe (w) + $FeAl_2O_4$ + Al_2O_3	10	$FeAl_2O_4$ + Al_2O_3	443 ± 80	3.0 ± 0.2	1542 ± 30
R22S	Fe + $FeAl_2O_4$ + Al_2O_3	65	$FeAl_2O_4$ + Al_2O_3	502 ± 70	3.4 ± 0.3	1650 ± 40
R72S	Fe + $FeAl_2O_4$ (w) + Al_2O_3	110	Fe + $FeAl_2O_4$ + Al_2O_3	524 ± 70	3.8 ± 0.3	2000 ± 50
R100S	Fe + Al_2O_3	–	Fe + Al_2O_3	695 ± 20	4.5 ± 0.3	1730 ± 30

SPS treatment, thus ruling out any formation of $FeAl_2O_4$ by oxidation of the Fe nanoparticles.

For the last part of the study, all four materials were prepared by SPS again, but in the form of pellets with a higher diameter (20 mm) in order to perform some mechanical tests. Note that the grinding and polishing processes completely eliminated the surface layer for R0S, but not for R22S and R72S. Therefore, the mechanical data for R0S will represent those of the core of the material. The indentation tests (10 N for 10 s in air at room temperature) were performed on the polished surface of the specimens by loading with a Vickers indenter (Shimadzu HMV 2000). The calculated microhardness values (Table 2) are the average of 10 measurements. HV is the lowest for R0S, showing that the composite layers formed by SPS for R22S and R72S are harder than the core material. The fact that HV is higher for R72S (2000) than for R100S (1730) could reflect a particular microstructure for the former. The transverse fracture strength (σ_f) was determined by the three-point bending test on specimens $1.6 \times 1.6 \times 18\ mm^3$ machined with a diamond blade. The cross-head speed was fixed at $0.1\ mm\ min^{-1}$. σ_f (Table 2) increases from R0S to R100S, which could reflect firstly (from R0S to R22S) the influence of the composite layer, and secondly (from R72S to R100S) the presence of $FeAl_2O_4$ decreasing to zero in the surface layer. The fracture toughness (K_{Ic}) was measured by the single-edge notched bending (SENB) method on similar specimens notched using a 100 μm SiC wire. A calibration factor [20] was used to calculate the SENB toughness from the experimental results. K_{Ic} (Table 2) increases from R0S to R100S, which could reflect the presence of $FeAl_2O_4$ decreasing to zero in the core of the materials. Indeed, the notch is deep enough so that only the core is tested. Note that the values for R100S ($\sigma_f = 695$ MPa and $K_{Ic} = 4.5\ MPa\ m^{1/2}$) are markedly higher than for the other materials. σ_f is similar to what is found for the hot-pressed Fe-Al_2O_3 nanocomposites, whereas K_{Ic} is lower [12,13], which could reflect differences in the microstructure and warrants further studies.

In conclusion, it has been shown for the first time that the sintering by SPS of partially reduced metal-oxide nanocomposite powders produces nanocomposite materials with a surface layer composition and microstructure different to that of the core of the material. The layer thickness is controlled in the range 10–110 μm. The applied SPS treatment induces reactions resulting in the formation of $FeAl_2O_4$, which may in turn produce Fe. The most severe reducing conditions are found at the surface of the materials which could be due to their insulating nature, which does not allow the electron flow to pass through the core. Only the fully reduced 7 wt.% Fe–Al_2O_3 powder is sintered without any reaction taking place. All materials are densified to 98–100%. The in situ formed composite surface layer favors a higher hardness and fracture strength. Future works, including the study of the influence of the SPS parameters and the investigation of the tribological properties of such surface-tailored nanocomposites, will be reported elsewhere.

The authors thank L. Datas for assistance in the TEM observations, performed at TEMSCAN, the "Service Commun de Microscopie Electronique à Transmission", Université Paul-Sabatier. The SPS was performed at the Plateforme Nationale CNRS de Frittage-Flash (PNF^2, Toulouse). The authors thank J. Faber and Y. Paranthoen (Société des Céramiques Techniques, Bazet, France) for the use of a H_2 furnace and a doctoral thesis grant for J.G.S. This work is performed under the programme ANR-06-NANO-049.

[1] M. Tokita, J. Soc. Powder Tech. Jpn. 30 (1993) 790.
[2] V. Mamedov, Powder Metall. 45 (2002) 322.
[3] Z. Shen, M. Nygren, Key Eng. Mater. 247 (2003) 79.
[4] A. Munir, U. Anselmi-Tamburini, M. Ohyanagi, J. Mater. Sci. 41 (2006) 763.
[5] A. Chesnaud, C. Bogicevic, F. Karolak, C. Estournès, G. Dezanneau, Chem. Commun. (2007) 1550.
[6] C. Elissalde, C. Estournès, M. Maglione, J. Am. Ceram. Soc. 90 (2007) 973.
[7] D. Oquab, C. Estournes, D. Monceau, Adv. Eng. Mater. 9 (2007) 413.
[8] U-Chan Chung, C. Estournès, C. Elissalde, M. Paté, J.P. Ganne, M. Maglione, Appl. Phys. Lett. 92 (2008) 042902/1.
[9] R. Chaim, M. Levin, A. Shlayer, C. Estournès, Adv. Appl. Ceram. 107 (2008) 159.
[10] X. Devaux, Ch. Laurent, A. Rousset, Nanostruct. Mater. 2 (1993) 339.
[11] Ch. Laurent, A. Rousset, M. Verelst, K.R. Kannan, A.R. Raju, C.N.R. Rao, J. Mater. Chem. 5 (1993) 513.
[12] X. Devaux, Ch. Laurent, M. Brieu, A. Rousset, C. R, Acad. Sci. Paris, Série II 312 (1991) 1425.
[13] Ch. Laurent, X. Devaux, A. Rousset, J. High Temp. Chem. Process. 3 (1994) 489.
[14] U. Anselmi-Tamburini, J.E. Garay, Z.A. Munir, A. Tacca, F. Maglia, G. Chiodelli, G. Spinolo, J. Mater. Res. 19 (2004) 3263.
[15] Ch. Laurent, Ch. Blaszczyk, M. Brieu, A. Rousset, Nanostruct. Mater. 6 (1995) 317.
[16] X. Devaux, Ch. Laurent, M. Brieu, A. Rousset, J. All. Comp. 188 (1992) 179.
[17] W.F. Brown, J.E. Srawley, ASTM Spec. Tech. Pub. 410 (1966) 13.
[18] Y. Makino, New Ceramics 10 (1997) 39.
[19] H. Tomino, H. Watanabe, Y. Kondo, J. Jpn. Soc. Powd. Metall. 44 (1997) 974.
[20] U. Anselmi-Tamburini, S. Gennari, J.E. Garay, Z.A. Munir, Mater. Sci. Eng. A394 (2005) 139.